

Numerical study of spectral shaping in high energy Ho:YLF amplifiers

Peter Kroetz,^{1,2,*} Axel Ruehl,³ Krishna Murari,^{1,3,4} Huseyin Cankaya,^{1,3,5} Franz X. Kärtner,^{1,3,4,5} Ingmar Hartl,³ and R. J. Dwayne Miller^{1,2,5,6}

¹Center for Free-Electron Laser Science (CFEL), Notkestraße 85, D-22607 Hamburg, Germany

²Max-Planck Institute for the Structure and Dynamics of Matter (MPSD), Luruper Chaussee 149, 22761 Hamburg, Germany

³Deutsches Elektronen-Synchrotron (DESY), Notkestrasse 85, 22607 Hamburg, Germany

⁴Department of Physics, University of Hamburg, 22761 Hamburg, Germany

⁵Centre for Ultrafast Imaging (CUI), Universität Hamburg, Luruper Chaussee 149, 22761 Hamburg, Germany

⁶Departments of Chemistry and Physics, University of Toronto, Toronto M5S 1A7, Canada

*peter.kroetz@mpsd.mpg.de

Abstract: We present a new chromatic numerical approach to simulate the amplification of laser pulses in multipass laser amplifiers. This enables studies on spectral effects such as gain narrowing and spectral shaping with optical elements expressed by a transmission transfer function. We observe good agreement between our simulations and measurements with a Ho:YLF regenerative amplifier (RA). To demonstrate the capabilities of our simulation model, we numerically integrate an intra-cavity etalon in this laser and find optimum etalon parameters that enhance the peak power of the output pulses up to 65%.

©2016 Optical Society of America

OCIS codes: (140.3580) Lasers, solid-state; (140.3430) Laser theory; (320.7090) Ultrafast lasers.

References and links

1. A. D. DiChiara, S. Ghmire, D. A. Reis, L. F. DiMauro, and P. Agostini, *Strong-field and Attosecond Physics with Mid-infrared Lasers in Attosecond Physics* (Springer-Verlag, 2013), pp. 81–98.
2. K.-H. Hong, C.-J. Lai, J. P. Siqueira, P. Kroger, J. Moses, C.-L. Chang, G. J. Stein, L. E. Zapata, and F. X. Kärtner, “Multi-mJ, kHz, 2.1 μm optical parametric chirped-pulse amplifier and high-flux soft x-ray high-harmonic generation,” *Opt. Lett.* **39**(11), 3145–3148 (2014).
3. M. Hemmer, D. Sánchez, M. Jelínek, V. Smirnov, H. Jelinkova, V. Kubeček, and J. Biegert, “2- μm wavelength, high-energy Ho:YLF chirped-pulse amplifier for mid-infrared OPCPA,” *Opt. Lett.* **40**(4), 451–454 (2015).
4. L. von Grafenstein, M. Bock, D. Ueberschaer, U. Griebner, and T. Elsaesser, “Picosecond 34 mJ pulses at kHz repetition rates from a Ho:YLF amplifier at 2 μm wavelength,” *Opt. Express* **23**(26), 33142–33149 (2015).
5. P. Kroetz, A. Ruehl, G. Chatterjee, A.-L. Calendron, K. Murari, H. Cankaya, P. Li, F. X. Kärtner, I. Hartl, and R. J. D. Miller, “Overcoming bifurcation instability in high-repetition-rate Ho:YLF regenerative amplifiers,” *Opt. Lett.* **40**(23), 5427–5430 (2015).
6. S. Klingebiel, C. Wandt, C. Skrobol, I. Ahmad, S. A. Trushin, Z. Major, F. Krausz, and S. Karsch, “High energy picosecond Yb:YAG CPA system at 10 Hz repetition rate for pumping optical parametric amplifiers,” *Opt. Express* **19**(6), 5357–5363 (2011).
7. C. P. J. Barty, G. Korn, F. Raksi, C. Rose-Petrucci, J. Squier, A.-C. Tien, K. R. Wilson, V. V. Yakovlev, and K. Yamakawa, “Regenerative pulse shaping and amplification of ultrabroadband optical pulses,” *Opt. Lett.* **21**(3), 219–221 (1996).
8. P. Malevich, G. Andriukaitis, T. Flöry, A. J. Verhoef, A. Fernández, S. Ališauskas, A. Pugžlys, A. Baltuška, L. H. Tan, C. F. Chua, and P. B. Phua, “High energy and average power femtosecond laser for driving mid-infrared optical parametric amplifiers,” *Opt. Lett.* **38**(15), 2746–2749 (2013).
9. K. Murari, H. Cankaya, P. Kroetz, G. Cirimi, P. Li, A. Ruehl, I. Hartl, and F. X. Kärtner, “Intracavity gain shaping in millijoule-level, high gain Ho:YLF regenerative amplifiers,” *Opt. Lett.* **41**(6), 1114–1117 (2016).
10. K. Yamakawa, M. Aoyama, S. Matsuoka, H. Takuma, D. N. Fittinghoff, and C. P. J. Barty, “Ultrahigh-peak and high-average power chirped-pulse amplification of sub-20-fs pulses with Ti:Sapphire amplifiers,” *IEEE J. Sel. Top. Quantum Electron.* **4**(2), 385–394 (1998).
11. W. F. Krupke and L. L. Chase, “Ground-state depleted solid-state lasers: principles, characteristics and scaling,” *Opt. Quantum Electron.* **22**(S1), S1–S22 (1990).
12. A. Dergachev, “High-energy, kHz-rate, picosecond, 2- μm laser pump source for mid-IR nonlinear optical devices,” *Proc. SPIE* **8599**, 85990B (2013).

13. L. M. Frantz and J. S. Nodvik, "Theory of pulse propagation in a laser amplifier," *J. Appl. Phys.* **34**(8), 2346–2349 (1963).
14. W. Koechner, *Solid-State Laser Engineering*, 4th ed. (Springer-Verlag, 1996), pp. 158–183.
15. P. Raybaut, F. Balembois, F. Druon, and P. Georges, "Numerical and experimental study of gain narrowing in Ytterbium-based regenerative amplifiers," *IEEE J. Quantum Electron.* **41**(3), 415–425 (2005).
16. A. E. Siegman, *Lasers* (University Science Books, 1986), p. 14.
17. R. B. Barthem, R. Buisson, J. C. Vial, and H. Harmand, "Optical properties of Nd³⁺ pairs in LiYF₄-existence of a short range interaction," *J. Lumin.* **34**(6), 295–305 (1986).
18. K. Mecseki, D. Bigourd, S. Patankar, N. H. Stuart, and R. A. Smith, "Flat-top picosecond pulses generated by chirped spectral modulation from a Nd:YLF regenerative amplifier for pumping few-cycle optical parametric amplifiers," *Appl. Opt.* **53**(10), 2229–2235 (2014).
19. E. Sorokin, G. Tempea, and T. Brabec, "Measurement of the root-mean-square width and the root-mean-square chirp in ultrafast optics," *J. Opt. Soc. Am. B* **17**(1), 146–150 (2000).
20. O. J. P. Collet, "Modeling of end-pumped Ho:YLF amplifiers," M.Sc. thesis (University Stellenbosch, 2013).

1. Introduction

Ho:YLF laser amplifiers with output pulse durations on the order of few-picoseconds are of increasing interest as mid-infrared (mid-IR) driving sources for manifold applications, such as in strong field physics [1], high-harmonic generation [2] and the generation of ultrafast pulses in the mid- and far-IR by optical parametric amplification [3]. Laser amplifiers based on the gain medium Ho:YLF are of particular interest due to its high gain cross section at the wavelength of 2.05 μm , its capability to store high energies and low quantum defect that altogether allows efficient amplification of low energetic seed pulses to multi-mJ pulse energies [3–5]. It was observed that in regenerative amplifiers (RA) during the amplification of low-energetic seed pulses to multi-mJ pulse energies, the spectral bandwidth narrowed down to ~ 2.5 , resulting in Fourier limited (FL) pulse durations of ~ 2.5 ps. As the aforementioned applications typically benefit from shorter pulses, numerical tools that can simulate the spectral evolution during pulse amplification can be crucial to optimize the pulse duration and the peak power of the driving laser systems.

In the past, spectral filters were successfully employed in laser amplifiers to reduce gain narrowing and achieve spectrally broadened output pulses. These filters were either positioned in front of the amplifier to spectrally pre-shape the seed pulses [6] or within the amplifier to shape the pulses during their amplification [7]. By spectrally pre-shaping the seed pulses of a Ho:YAG RA, the compressed output pulses were shortened from ~ 3.5 ps to ~ 530 fs [8]. More recently, intra-cavity spectral shaping with an intra-cavity etalon in a Ho:YLF RA was demonstrated and the spectral FWHM of the output pulses was increased from 2.9 nm to 5.4 nm [9]. In particular for systems with high single pass gains, which typically is the case for Ho:YLF RAs, using an intra-cavity etalon is a simple and affordable technique. As the etalon shapes the pulse spectrum many times during amplification, the amount of spectral shaping per shaping event can be moderate. The amount of spectral shaping, which is a function of the etalon surface reflection, can be controlled by selecting certain types of glasses that directly provide the required amount of spectral shaping due to their Fresnel reflections, as demonstrated in [9], and no additional AR coatings are necessary. In contrast, if the spectral shaping is only applied one time to the seed pulses before their amplification, the required amount of spectral shaping is very high and not in all cases easy to control experimentally. Therefore, spectral pre-shaping techniques seem to be more applicable for laser amplifiers with low- and medium total gains.

In this paper we present a spectral simulation model that allows us to simulate the amplification in Ho:YLF laser amplifiers and to study gain narrowing in such systems. The underlying equations are based on Franz-Nodvik equations that we generalized for the spectral regime to account for chromatic effects. The same set of equations was used for the simulation of the pumping process by accounting for the inversion decay losses during the pumping times. The presented simulation method can be computed in less time as compared to simulation methods that involve numerically more complex rate equations [10]. This is of particular importance for example to statistically analyze the noise and bifurcation behavior of RAs, or to finely sample certain parameters over a wide parameter space. In the context of

studying gain narrowing and compensation thereof, we have chosen to numerically implement an etalon as an example case for a spectral intra-cavity filter into a Ho:YLF RA. We identify an optimum etalon for the system and our simulations predict a peak power enhancement of up to 65%.

The paper is organized as follows. In the first part, we review Ho:YLF as a gain material with respect to the spectral emission and absorption cross sections and identify the range of inverted fractions between which a Ho:YLF laser amplifier operates. Afterwards we describe our simulation approach, including the underlying spectral equations and the framework of the simulation program. In the second part of the paper, we demonstrate the capability of our simulation method and numerically insert an etalon into a Ho:YLF regenerative amplifier and vary the etalon parameters thickness, surface reflection and turning angle to identify optimized etalon parameters with regard to enhanced peak power of the output pulses.

In this paper, we will use the term inverted fraction β as a measure of the inversion in the gain medium. The inverted fraction is defined as [11]

$$\beta = \frac{n_e}{N_{total}}, \quad (1)$$

with n_e representing the number of excited ions and N_{total} the total number of ions in the considered gain volume. Figure 1(a) shows the effective two-level absorption and emission cross sections of Ho:YLF in the wavelength range from 1.9 μm to 2.1 μm at room temperature [12]. The spectral gain cross sections for three different inverted fractions are shown in (b). Values of the inverted fraction of 55.5% (representing full gain saturation at the pump wavelength) and 24.7% (representing full gain depletion at the seed wavelength) act as the boarder values between which a Ho:YLF RAs pumped at 1.94 μm and seeded at 2.05 μm can operate. Negative or positive gain cross sections imply absorption or amplification of the associated wavelength, whereas a zero represents a transparent gain medium. During the pumping or amplification process, the gain cross sections increase or decrease, respectively, with a limiting value of zero that represents complete gain saturation at the pump wavelength or complete gain depletion at the seed wavelength. It has to be noted, that depending on the pump power and the amplifying conditions, the value-pair of the inverted fraction after the pumping and after the amplification process can lay everywhere in between the mentioned boarder values.

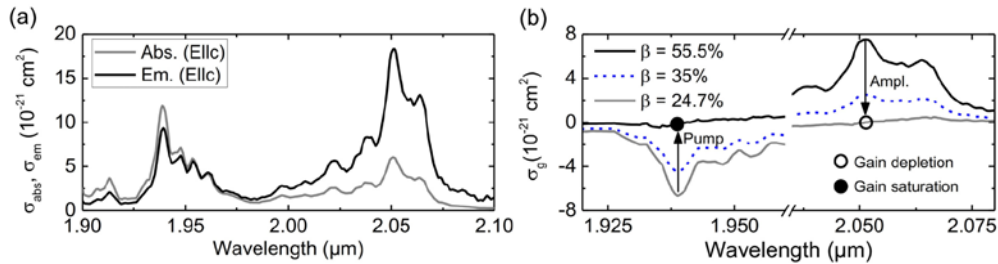


Fig. 1. (a) Absorption and emission cross sections σ_{abs} and σ_{em} of Ho:YLF [12] at room temperature. (b) Gain cross sections σ_g for different inverted fractions. Values below and above zero cause absorption and amplification, respectively. Calculated with Eq. (3) and the cross sections from (a).

2. Introduction chromatic simulation code

The classical Frantz-Nodvik (FN) formalism is a common approach to simulate monochromatic pulse amplification in a gain medium [13]. Its validity holds until the amplification time is short as compared to the excited ions lifetime in the gain medium. The classical FN equations are explained in [14]. Due to its monochromatic nature, the classical FN formalism cannot be used to study spectral effects such as gain narrowing. A previous

attempt to transfer the FN equations into a chromatic version is based on the definition of a spectral stored fluence and its calibration with monochromatic values of the saturation fluence and the small signal gain [15]. With that approach, however, we were not able to reproduce the experimental results from our Ho:YLF regenerative amplifier, neither spectrally nor energetically. Hence we reformulated the classical FN equations that update the gain in the gain medium to equivalent expressions that update the inverted fraction.

Figure 2 compares the classical FN formalism with our modified approach. In the classical FN formalism, sketched in Fig. 2(a), an initial small signal gain g_{i-1} is used to calculate the amplification or absorption of an incoming fluence J_{i-1} . With the change in the fluence ΔJ_{i-1} and by defining a stored fluence $J_{\text{stor},i-1}$ in the gain medium, the new small signal gain g_{i-1} can be calculated which is then used in the consecutive pass to simulate further amplification. After each pass, the stored fluence $J_{\text{stor},i-1}$ is lowered by the extracted fluence ΔJ_i to conserve the energy in the system. Although the definition of a stored fluence J_{stor} for monochromatic FN simulations is adequate, the analogous definition of a spectral stored fluence $J_{\text{stor}}(\lambda)$ is difficult, as the energy conservation is not directly fulfilled, which led to the calibration of spectral values in the aforementioned approach [15]. Our modified approach presented in Fig. 2(b) circumvents the expression of a stored fluence and can be directly transferred to the generalized equations for the spectral regime. Owing to the direct relation between the inverted fraction of the gain medium β and the extracted fluence ΔJ , the energy is conserved with our approach. For monochromatic simulations, both approaches are completely equivalent.

The advantage of updating the inverted fraction instead of the gain is that, under the assumption of homogeneous broadening, the inverted fraction can be considered as wavelength independent, whereas the gain always has a spectral dependence, as shown in Fig. 1(b). Purely homogeneous broadening can be found in solid state laser gain materials with an isotropic distribution of the dopant ions resulting in single energetic transition energies [16,17]. Berthem et al. observed that crystal distortions in YLF doped with the lanthanide Neodymium show small inhomogeneous broadening, indicated by a small energy splitting of $< 1 \text{ cm}^{-1}$ [17]. We assume the energy splitting in YLF doped with the lanthanide Holmium on the same order of magnitude and, thus, assume only homogeneous broadening in our simulations. This is supported by the fact that we did not observe inhomogeneous broadening effects, such as spectral hole burning, during operation of Ho:YLF RAs.

To simulate homogeneous broadening, we operate as follows. Prior to each amplification or pump pass, we temporally divide the incoming pump or seed fluence by slicing it into smaller fluence slices. The propagation of each slice through the gain medium is consecutively simulated and after each propagated slice the inverted fraction is updated. The updated inverted fraction is then used to simulate the propagation of the following fluence slice. This procedure is explained in Fig. 3. We observed that slicing the seed and pump fluence into 10 temporally divided fluence slices reproduced the results of our CW pumped, 1 kHz repetition-rate Ho:YLF regenerative amplifier presented in [9].

We furthermore modified the FN equations to include inversion decay losses during the fluence propagation time and we, therefore, use the same set of equations for the simulation of the pump and amplification process. In this context, slicing of the pump fluence is also crucial to correct for the inversion decay losses during long CW pumping times.

The saturation fluence in Ho:YLF at $2.05 \text{ }\mu\text{m}$ is $\sim 4 \text{ J/cm}^2$, which for example is reached with a focal diameter of 1 mm at a pulse energy of 31 mJ. Consequently, for chirped pulses with energies only in the few-mJ regime, the front part of the pulses cannot deplete the gain during



Fig. 2. Comparison of (a) the classical and (b) the modified FN equations. While the classical equations define and utilize a stored fluence J_{stor} the modified equations circumvent this expression by using the inverted fraction β .

its amplification. In our simulations we, therefore, can work with unchirped pulses realized by assigning the same spectral content to each fluence slice. Similarly, we do not expect that dispersion effects, which induce a rather small pulse chirping (dispersion length ~ 22 m for a 1-ps pulse at $2 \mu\text{m}$ in Ho:YLF), play a role in the amplification in Ho:YLF RAs. However, if required, the amplification of chirped pulses and dispersion effects could be tackled by varying the spectral content from slice to slice (spectral distribution then is based on the spectral phase that needs to be defined additionally) and a transfer function that allows the exchange of spectral components between slices during amplification. The B-integral in the here simulated system is assumed to always stay below 1. As also for Ho:YLF RAs with B-integrals above 1, no nonlinear effects were reported [5], no attempt has been made to include nonlinear effects to the simulation model:

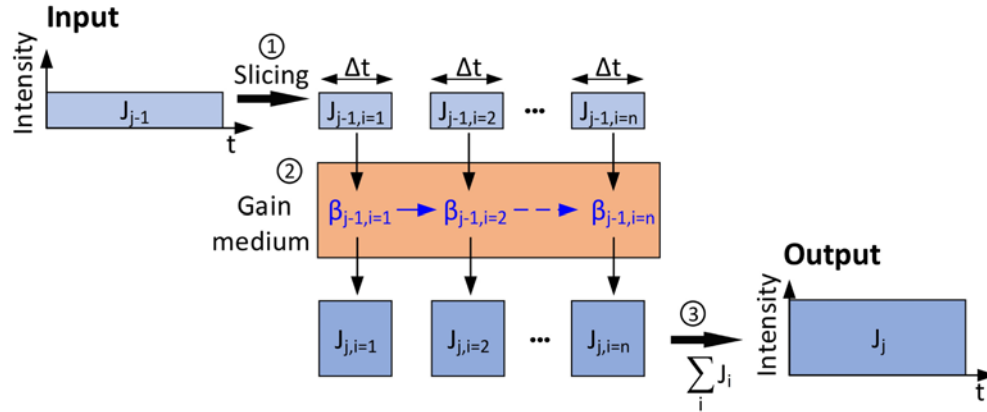


Fig. 3. Simulation of a single pass of the fluence J_{i-1} through a gain medium. (1): The incoming fluence is sliced into n equal fluence slices. (2): Each fluence slice consecutively passes the gain medium, in which the inverted fraction β is updated between the passes. (3): The sum of all fluence slices results in the total output fluence.

3. The spectral FN-equations

In the following, we will only outline the main equations needed for our simulation model. The full derivation of the inverted fraction updating equation, starting from the classical gain updating equation, can be found in Appendix 1. Additionally in Appendix 2, Table 1 lists all symbols and parameters used in this paper. Analogous to the monochromatic single pass gain, we express the spectral single pass gain or single pass absorption, respectively, $G_{i-1}(\lambda)$ as

$$G_{i-1}(\lambda) = \exp(\sigma_{g,i-1}(\lambda)Nl), \quad (2)$$

with the spectral gain cross section

$$\sigma_{g,i-1}(\lambda) = \beta_{i-1}(\sigma_{em}(\lambda) + \sigma_{abs}(\lambda)) - \sigma_{abs}(\lambda), \quad (3)$$

where β_{i-1} represents the averaged global inverted fraction, $\sigma_{em}(\lambda)$ and $\sigma_{abs}(\lambda)$ the emission and absorption cross sections, N the dopant ion density in the gain medium and l the length of the

gain medium. After the first pass of an initial spectral fluence $J_{i-1}(\lambda)$ through the gain medium, the amplified or remaining spectral fluence after the passage $J_i(\lambda)$ can be calculated as

$$J_i(\lambda) = J_{sat}(\lambda)T(\lambda)\ln\left(1 + G_{i-1}(\lambda)\exp\left(\frac{J_{i-1}(\lambda)}{J_{sat}(\lambda)}\right) - 1\right), \quad (4)$$

with the saturation fluence

$$J_{sat}(\lambda) = \frac{hc}{\lambda(\sigma_{abs}(\lambda) + \sigma_{em}(\lambda))}, \quad (5)$$

where c represents the speed of light, h the Planck constant and $T(\lambda)$ the single pass transmission to account for a global loss. Equation (3) and (4) are analogous to the classical monochromatic expressions, but in the next step, instead of updating the gain, we update the inverted fraction β with

$$\beta_i = \beta_{i-1} - \frac{\int \left[\lambda \left(\frac{J_i(\lambda)}{T(\lambda)} - J_{i-1}(\lambda) \right) \right] d\lambda}{hclN}. \quad (6)$$

4. Modelling pumping processes with FN formalism

Since, fundamentally, there is no difference between amplification or absorption (neglecting amplified spontaneous emission), the FN equations are also valid for absorption with the same limitation concerning the upper laser level lifetime. In order to use these equations to simulate long continuous-wave (cw) pumping processes, a further small modification was necessary to account for the inversion decay losses during the pumping time. As the amplification process in regenerative amplifiers usually happens on much faster time scales, this correction can be neglected for the simulation of amplification. We corrected the inverted fraction after each pass of sliced pump fluence with

$$\beta_i^* = \beta_i \exp\left(-\frac{\Delta t}{\tau_{gain}}\right), \quad (7)$$

where τ_{gain} represents the upper laser level lifetime, which is 15 ms in the case of Ho:YLF [12], and Δt is the time duration of the sliced fluence. It has to be noted, that the expression $\exp(-\Delta t/\tau_{gain})$ is not derived from the previous equations but is added adjacently as a correction factor on the basis of the knowledge of the inversion decay law [16]. This correction factor is necessary for pumping processes with pumping times close to and longer than the excited ions lifetime. The effect of this correction is presented in Fig. 4(a), showing the time-resolved build-up of the inverted fraction in a 1 cm long Ho:YLF crystal that is pumped with 50 W linearly polarized light. The beam diameter was set to 1 mm. The figure compares the build-up calculated with monochromatic FN equations, with and without inversion correction, and with monochromatic quasi-three level rate equations [20]. The curves computed with the rate equations and the inversion-corrected FN equations are nearly identical. To estimate the validity of the corrected FN equations for other gain materials we numerically varied the upper laser level life time. We present in (b) and (c) results for the same set of simulation parameters used in (a) but with decreased life times of 7 ms and 1 ms. For a life time of 7 ms, we still observe good agreement between the results from the rate equations and the corrected FN equations, while for 1 ms, the corrected FN equations overestimate the effect of the inversion decay losses. In this particular case, the inverted fraction values calculated with the corrected FN equations are 15% lower than the values calculated with rate equations. However, this discrepancy also depends on the pump power. For example, when increasing the pump power in the 1 ms life time case to 100 W, the

difference between the inverted fraction values after 2 ms of pumping is $< 4\%$. In this particular case, the advantage of the FN equations over the rate equations is a significantly reduced computation time.

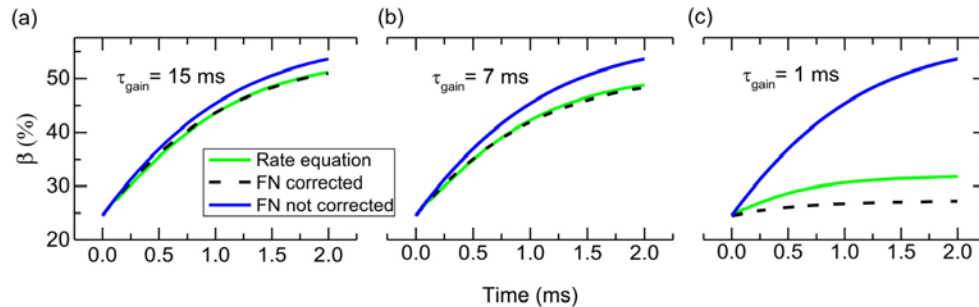


Fig. 4. (a) Comparison between the build-up of the inverted fraction β simulated with rate equations and FN equations with and without correction of the inversion decay losses. To evaluate the effect of the life time, (b) and (c) presents simulation results with varied life times.

5. Flow-chart of the simulation program

To simulate consecutive pump and amplification cycles, the above introduced formalism was integrated into a Matlab written framework, which is shown in Fig. 5 as a flow-chart. Starting with a random initial inverted fraction β_0 , the model simulates consecutive pump and amplification cycles, sketched out in Fig. 5(a). For operation in stable operation regimes, we observed that after a few cycles the system always converges towards the same results, independent from the initially chosen value for the inverted fraction. For the pumping process, we consider a single pass of the pump fluence through the gain medium. In contrast, for the amplification process we simulated N round trips, corresponding to $2N$ single passes. Since the model considers consecutive cycles, this scheme also allows analyzing system properties such as the noise and stability of the output pulses including its susceptibility to show bifurcation. Recently, an identical scheme was employed to closely reproduce a complete bifurcation trajectory of a 1 kHz, Ho:YLF regenerative amplifier, albeit using the monochromatic FN formalism [5].

Figure 5(b) presents the underlying framework for a single pump or amplification process. The incoming fluence is sliced and each slice individually passes through the gain medium. In

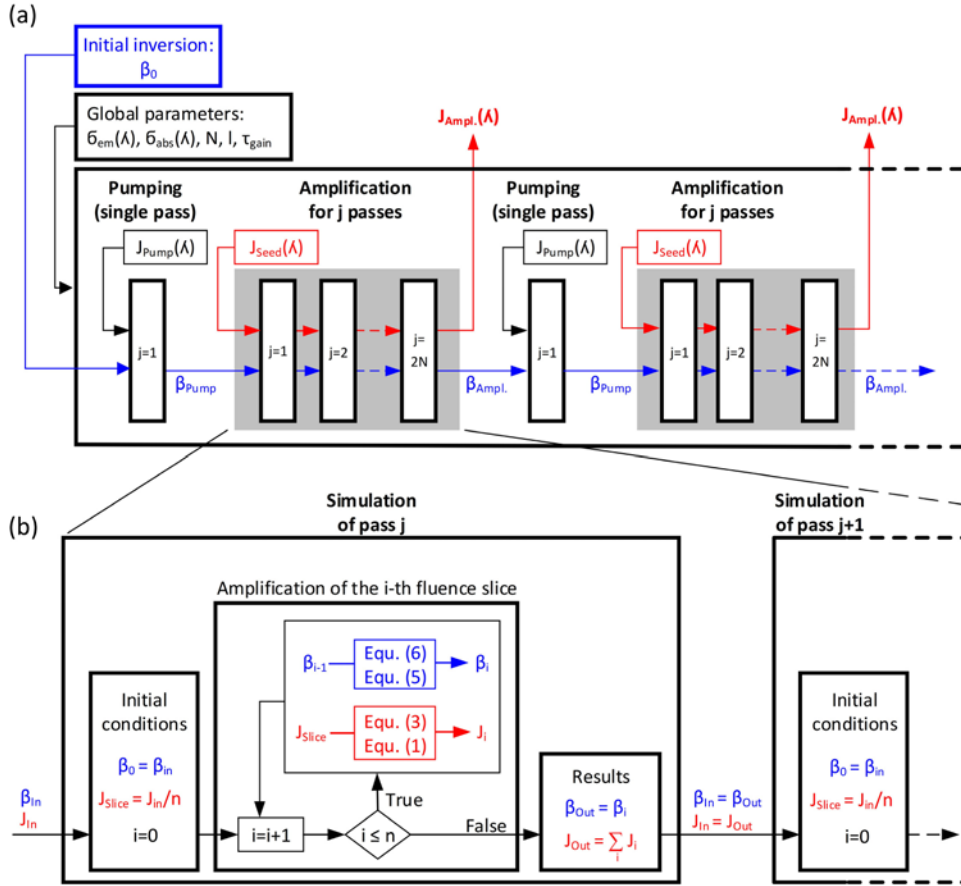


Fig. 5. (a) Flow-chart for consecutive pump and amplification cycles. For single pass pumping, the pump fluence only passes once the gain medium, whereas the seed fluence is amplified for $2N$ amplification passes (N round trips). (b) The incoming seed or pump fluence is sliced into n slices and each slice individually passes the gain medium. After each slice, the inverted fraction is consecutively updated.

the gain medium the fluence is either absorbed or amplified and consequently, the inverted fraction increases or decreases. Although Fig. 5(b) explicitly lays out the simulation procedure for an amplification pass, the procedure for the pumping process is identical, and we therefore omit to sketch it out.

6. Modeling of an intra-cavity etalon

Our model can account for arbitrary spectral shaping mechanisms that can be represented by a spectral single pass transmission $T(\lambda)$. The wavelength dependent etalon transmission $T_{etalon}(\lambda)$ was modeled as a function of the surface reflection R , the etalon thickness L and the etalon angle Θ [18]

$$T_{etalon}(\lambda) = \frac{1}{1 + \frac{4R}{(1-R)^2} \sin^2\left(\frac{\pi}{\lambda} nL \cos(\Theta)\right)}, \quad (8)$$

with n representing the refractive index of the etalon material. The etalon can be implemented as an additional wavelength dependent transmission loss in the Eqs. (3) and (5) via

$$T^*(\lambda) = T(\lambda)T_{etalon}(\lambda). \quad (9)$$

The experimental setup of the Ho:YLF RA discussed here is shown in Fig. 6(a) and the consecutive order of gain and spectral filtering elements in Fig. 6(b). First, the etalon is passed two times and each RT involves two passes through the gain medium and two passes through the etalon. Depending on the position of the spectral filter in the cavity, the consecutive order in which the gain shaping elements are passed during the amplification process might be different and needs to be considered accordingly. This approach is not restricted to intra-cavity shaping but can also be applied to spectrally pre-shape a laser pulse prior its in-coupling.

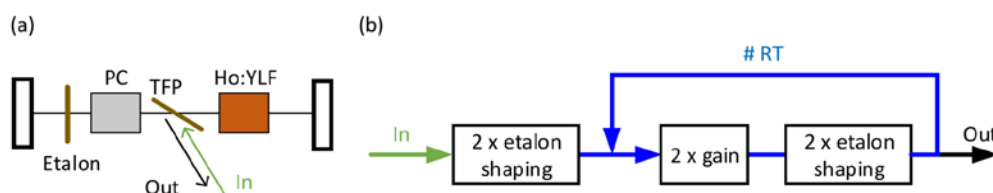


Fig. 6. (a) Setup of our Ho:YLF RA including intra-cavity etalon. (b) Consecutive order of passes through the gain shaping elements during amplification in the RA. TFP, thin film polarizer; PC, Pockels cell.

7. Validation of the simulation model

Figure 7 presents the measured and simulated output spectra of a Ho:YLF regenerative amplifier, without and with intra-cavity etalon. The etalon was turned such that the highest spectral losses were induced at the gain peak of Ho:YLF at 2.051 μm . This effectively reduced the amount of amplified spectral power at this wavelength in comparison to the spectral wings of the amplified pulse where fewer losses were induced by the etalon. To study the effect of the etalon surface reflection, two different glasses were used: UVSF with a refractive index of $n = 1.448$ and N-SK2 with a refractive index of $n = 1.583$, resulting in Fresnel surface reflections of 3.3% and 5.1%, respectively. This data was already presented in [9]. The simulations for the experiments there were conducted based on the method presented here. The output pulses were coupled out after 8 round trips. The pump power was adjusted to achieve output pulse energies of 0.5 mJ, a limit set by the damage thresholds of the optical components. Further details concerning the experimental setup and results can be found in the same reference. The simulation results are in good agreement with the experiments, although the spectral shaping effect of an intra-cavity etalon at the Ho:YLF gain peak at 2.051 μm is slightly overestimated in the simulations. The observed differences can be explained with deviations of the actual emission and absorption cross-sections from those used in the simulations. Furthermore, the etalon parameters thickness and surface reflection can deviate from the specified values. Finally, as Eq. (7) describes the transmission of a “perfect” etalon, imperfections in the etalon, such as a not perfect flatness, were not considered in the simulations. Measurements with a frequency-resolved optical gating setup revealed that the additional thin intra-cavity etalon did not cause additional distortions to the spectral phase.

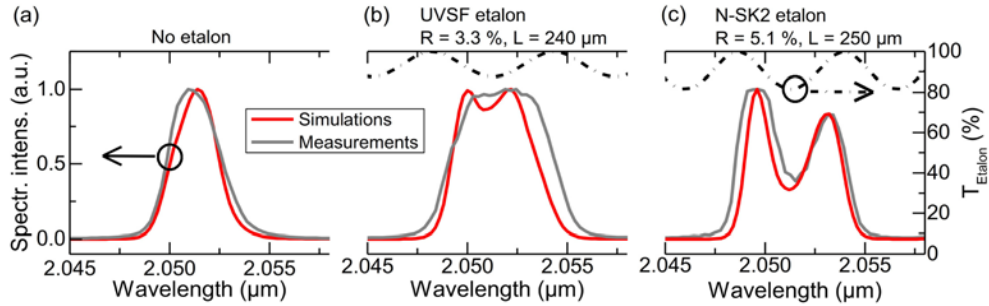


Fig. 7. (a) Measured and simulated output spectra of the Ho:YLF RA without intra-cavity etalon and (b) and (c) with different intra-cavity etalons. The black dash-dotted curve shows the transmission function of the etalon that was used for the corresponding simulation. Experimental data taken from [9].

8. Spectral simulation of pulse amplification in Ho:YLF RAs

For the simulations presented in the following we keep the simulation conditions as follows. The parameters that describe the Ho:YLF regenerative amplifier, such as crystal length, doping concentration and beam diameters, were taken from the RA system described in [9]. In our simulations, we neglect any noise from the pump and seed sources. We simulate nine consecutive pump and amplification cycles. To decouple the results from the starting conditions, we neglect the first six cycles and use the averaged output values from the last three cycles for the further analysis. Each pump and amplification cycle consists of a 1 ms long pump process (mimicking a repetition rate of 1 kHz) followed by the amplification of the seed pulses for 8 round trips. We assume single pass losses of 7.5%, which was found to be optimal to match the experimentally measured pulse energies of the considered RA, although this value is smaller than the measured single pass losses of 11%. For the simulations presented in Fig. 8, 9 and 10, we use a linear polarized pump power of 15.8 W, whereas, in Fig. 11 the pump power is varied. As pointed out in [15], the spectral gain is broader at lower inverted fraction values, which was shown in Fig. 1(b) for an inverted fraction of 55.5% (black curve) and 35% (dotted curve). As a consequence, the amplification of a pulse in a gain medium with the higher inverted fraction for a fixed number or round trips will result in a narrower spectral output. But, as the gain is higher, it also results in higher pulse energies.

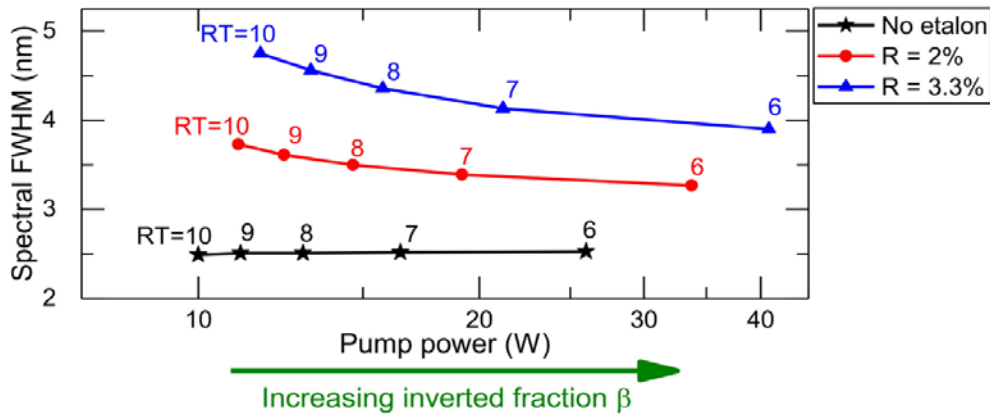


Fig. 8. Change in the spectral FWHM of the output pulses in dependence of the pump power for three different system configurations. Pulses are coupled out with a constant pulse energy of 0.5 mJ, which was adjusted by the the pump power and round trip number RT. An increased pump power follows an increased inverted fraction β in the gain medium. The numbers in the figure represent the number of round trip at which the pulses are coupled out.

For systems that are limited to certain maximum pulse energies, for example due to damage thresholds of optical components, it is important to know the amount of gain narrowing in dependence of the pump power and the number of round trips, while keeping the output pulse energy fixed. This is worked out in Fig. 8, for three system configurations, with and without intra-cavity etalons. Without an etalon, the spectral FWHM nearly stays constant, with the tendency towards higher values for higher pump powers. In this case, the increased gain narrowing due to an increased inverted fraction is slightly overcompensated by the switching out of the pulses at an earlier round trip number RT. In contrary, in the cases with an additional intra-cavity etalon, the spectral FWHM decreases with higher pump power at a fixed output pulse energy. This can be explained by the increased number of round trips needed at lower pump powers, which consequently leads, in total, to a stronger spectral shaping effect from the etalons.

9. Identification of optimum etalon parameters

Figure 9(a) and 9(d) present the spectral FWHM of the output pulses, sampled over a certain range in the parameter space that is accessible with an etalon. In (a) as a function of the etalon angle theta and the etalon thickness L, and in (d) as a function of theta and the surface reflection R. Figure 9(b) and 9(c) present vertical cuts, along theta, and horizontal cuts, along the thickness, through (a). As can be seen in 9(c), the spectral FWHM is periodic for the parameter thickness: About every 0.7 μm the spectral FWHM has a maximum. As the actual widths of these peaks are quite narrow (FWHM approx. 0.1 μm), it is experimentally difficult to obtain an etalon with a thickness that exactly matches the peak of the spectral FWHM. However, the spectral peak can be shifted sideways by the etalon angle theta. It is therefore important to note that by angle-tuning of theta it is always possible for any etalon thicknesses to find a spectral FWHM peak, as is presented in Fig. 9(b) for three different thicknesses.

These simulations were performed assuming a UVFS etalon (R = 3.3%). Therefore, at the spectral FWHM peaks, the spectral intensity profile looks like the simulated profile in Fig. 7(b). Figure 9(d) shows that the maximum spectral FWHM of the output pulses increases for higher surface reflections R, however at the same time the range in Θ over which the FWHM peak is accessible gets narrower. In (e), the spectral intensity profile is presented for the surface reflections 3.3% and 7%, which are marked in (d) with the two crosses. While the R = 3.3% etalon only causes a moderate spectral disturbance, the R = 7% etalon creates a significant dip at 2.051 μm. This spectral dip in the output spectrum causes side-wings in the calculated Fourier limited temporal pulse profile, that is shown in (e) for the two cases. Therefore, it is important to note that neither the spectral nor the temporal FWHM value of the output pulses can be an alone benchmark for their quality and, equally, they can neither be used for the identification of an optimized etalon. Here, we introduce in the following two definitions that we additionally use to evaluate the pulse duration and the pulse quality of the output pulses. In terms of the pulse duration we will use the root-mean-square (rms) duration that is defined in [19] as

$$\tau_{rms} = \sqrt{\langle t^2 \rangle - \langle t \rangle^2}, \quad (10)$$

$$\text{with } \langle t^n \rangle = \frac{1}{N} \int_{-\infty}^{\infty} t^n I(t) dt \text{ and } N = \int_{-\infty}^{\infty} I(t) dt,$$

where I(t) represents the temporal intensity profile of the pulse. The rms-pulse-duration-bandwidth-product is smallest for unchirped pulses and makes it to a good choice for example to evaluate the quality of pulse compression techniques. As τ_{rms} takes the energy content in the wings of a pulse into account, it is also a valuable measure for the pulse quality. However, to evaluate the pulse quality we define the normalized pulse contrast (NPC) with:

$$NPC = \frac{\tau_{FWHM}}{\tau_{rms} 2\sqrt{2\ln 2}} \approx \frac{\tau_{FWHM}}{\tau_{rms} 2.355}. \quad (11)$$

This definition provides a convenient and direct comparison to a reference pulse profile, which we have chosen to be Gaussian, represented by the scaling factor $2\sqrt{2\ln 2}$. Therefore, the NPC of a Gaussian pulse profile is 1. Pulses with more or less temporal content in the wings result in NPC values smaller or larger, respectively, than 1. Consequently, a square pulse has the max. possible NPC with a value of 1.47. A sech2 pulse has a NPC of 0.83.

Depending on the application of interest other definitions for the pulse quality might be more useful. In processes only triggered by intensities exceeding a certain threshold value, possible side wings might not be relevant, whereas in time-resolved pump probe measurements of sensitive systems the energy content in the side wings could have an adverse effect on the time resolution. Also other analysis methods could be considered, such as a momentum analysis.

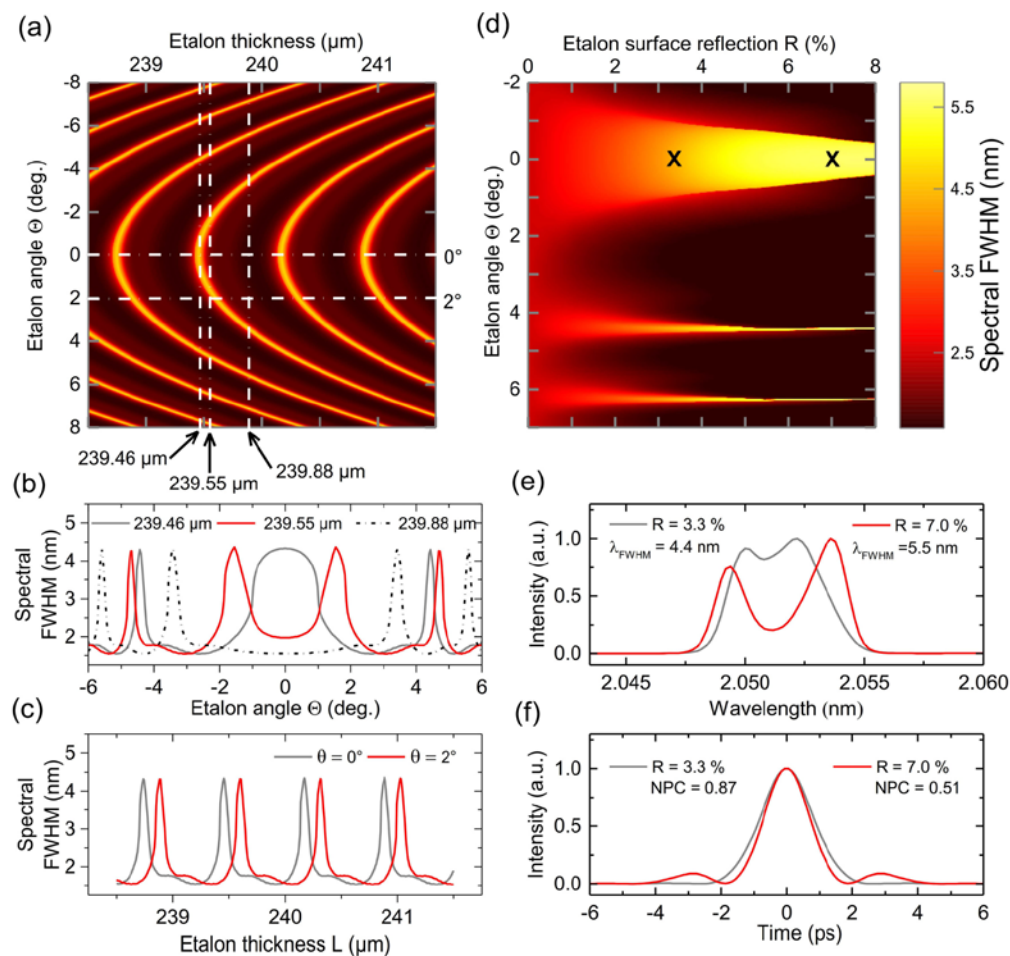


Fig. 9. (a) Parameter scan over the etalon parameters etalon thickness L and etalon angle Θ (for an etalon surface reflection of 3.3%) and (d) over surface reflection R and etalon angle (for an etalon thickness of 239.46 μm). Color represents the spectral FWHM λ_{FWHM} of the output pulses. Cuts through (a) along the etalon angle and along the etalon thickness are presented in (b) and (c), respectively. Two selected output spectra (marked with the two crosses in (d)) are presented in (e) and the calculated Fourier limited pulse shapes of these two spectra in (f).

In the example shown in Fig. 9(f), τ_{FWHM} is indeed decreased with the $R = 7\%$ etalon when comparing to the $R = 3.3\%$ etalon by 15% (1.58 ps vs 1.84 ps), but τ_{rms} increased by 44% (1.3 ps vs. 0.9 ps) due to the side wings, and consequently the NPC is significantly decreased by 39% (0.87 vs 0.51). To identify the optimum parameters for the considered Ho:YLF regenerative amplifier in regard to the etalon thickness and surface reflection, we sampled the etalon thickness from 1 μm to 300 μm in 15 000 equidistant steps, for the 4 etalon surface reflections 2%, 3.3%, 5% and 8%. For each surface reflection we receive a graph comparable to the one presented in Fig. 9(c). We omitted to sample the etalon angle as this does not lead to higher FWHM values for a given length and surface reflection value, as indicated in Fig. 9(b). For each simulation, we coupled the pulses out after 8 round trips, and the corresponding τ_{rms} of the Fourier limited pulse duration was calculated by taking the Fourier transform of the output spectrum, assuming a flat phase. With etalon thicknesses steps of 3 nm, the minimum τ_{rms} was selected and further analyzed concerning τ_{FWHM} and NPC. The results are shown in Fig. 10. For all surface reflections, the minimum τ_{FWHM} is located at etalon thicknesses of around 125 μm (see Fig. 10(a)). Within the simulated parameter range, higher surface reflections lead to a lower τ_{FWHM} . For example, with the $R = 8\%$ etalon, a minimum τ_{FWHM} of 1.3 ps was obtained, in contrast to 1.75 ps with the $R = 3.3\%$ etalon. However, the normalized pulse contrast NPC, presented in Fig. 10(b), has different optimum etalon thicknesses for each simulated surface reflection. While the optimum thickness for the $R = 8\%$ etalon is about 150 μm , for lower surface reflections, the optimum thickness shifts to larger thickness values. It is important to note, that for the simulations presented in Fig. 10, all amplification processes are simulated with a fixed pump power and a fixed number of round trips. As the different etalons induce different amounts of losses, the output pulse energy varies for each case.

One intention of this etalon study is to achieve an enhanced peak power of the output pulses, for which the pulse energy is an important factor. As the maximum pulse energy of the considered experimental system was limited to 0.5 mJ, due to damage threshold constraints, we therefore adjusted the pump power to achieve this pulse energy. We kept the number of round trips fixed, since we observed that an increase could lead to the onset of bifurcation. To calculate peak powers, we use τ_{rms} as the relevant measure of the pulse duration. In Fig. 11 we present results for the three different etalon thicknesses 150 μm , 200 μm and 240 μm , which we have identified as promising in Fig. 10 b). We omit to present results for the thickness 175 μm (peak of green curve in Fig. 10 (b)) due to space restrictions. For all thicknesses, τ_{FWHM} decreases for increasing etalon surface reflection. However, τ_{rms} reaches a minimum value at different surface reflections, which is also represented by a maximum NPC. The peak power of the output pulses increase from 0.46 GW (no etalon) up to 0.76 GW, 0.63 GW and 0.56 GW for the etalon thicknesses of 150 μm , 200 μm and 240 μm , which represents a peak power enhancement of 65%, 37% and 22%, respectively.

It has to be noted that for the simulated system, with output pulse energies on the order of 0.5 mJ, the gain is not depleted. However, if the number of round trips is further increased and higher output pulse energies are extracted, the spectral gain, in concert with the inverted fraction, is decreasing. Therefore, while the spectral gain and the spectral shaping strength may have compensated each other for a certain number of round trips, for larger numbers the spectral shaping effect of the etalon might become too prominent. The optimum etalon parameters for a given system, therefore, depend not only on the targeted output pulse energy and initial single pass gain, but also on the corresponding gain depletion level. In our simulations, for a fixed pump power we experienced that with an increasing etalon surface

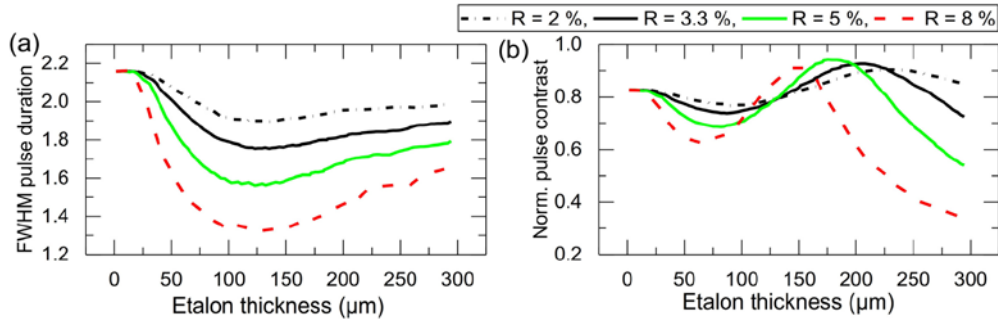


Fig. 10. (a) Calculated Fourier limited FWHM pulse duration as a function of the etalon thickness for 4 different surface reflections. (b) Normalized pulse contrast, as a measure for the pulse quality, for the same surface reflections.

reflection R the onset of bifurcation happens at lower output pulse energies. We attribute this to the additional losses that the etalon induces to the RA system.

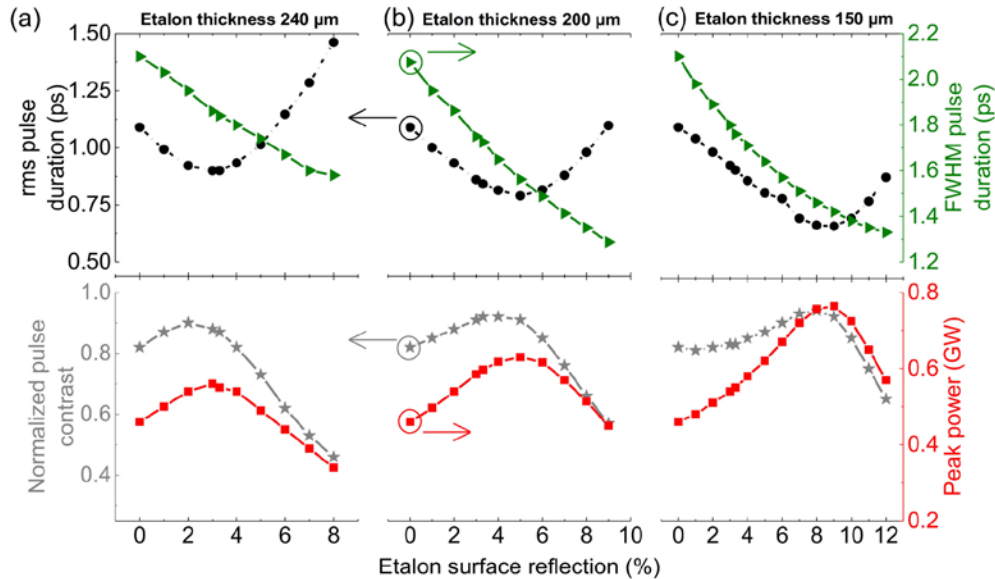


Fig. 11. Comparison of three etalon thicknesses (a) 240 μm, (b) 200 μm and (c) 150 μm as a function of the surface reflection. The analysis has been conducted in terms of the rms and FWHM pulse duration (upper row), and in terms of normalized pulse contrast and peak power (lower row).

10. Conclusions

In conclusion, we developed a simulation model that is capable of simulating amplification in pulsed Ho:YLF laser amplifiers while taking spectral effects in to account, such as gain narrowing and other chromatic effects. The underlying equations were derived from classical monochromatic Franz-Nodvik equations. We reformulated the classical equations that update the gain to equivalent expressions that eventually update the inverted fraction in the gain medium. The advantage of the reformulated expressions is that they could directly be transferred to and generalized for the spectral regime. A further modification allowed us to account for inversion decay losses in the gain medium and, consequently, we use the same set of equations also to simulate the pumping process of the gain medium. To benchmark our simulation model, we numerically inserted an intra-cavity etalon and found good agreement

between our simulations and experiments. One benefit of our simulation model is that it is computationally less expensive than approaches that are based on solving rate equations. This is of particular importance for simulations that involve wide parameter scans. As an example case, we chose to find optimum etalon parameters for a particular Ho:YLF RA. We Fourier transformed the simulated output spectra and analyzed the temporal pulse profile in terms of peak power enhancement and normalized pulse contrast. We found a peak power enhancement of up to 65%, for an etalon with a thickness of 150 μm and a surface reflection of 8%. The total amount of spectral shaping that an intra-cavity spectral filter induces depends on, first, geometrical parameters, such as the consecutive order that the pulses pass through spectrally active elements during their amplification and, second, gain related parameters such as the single pass gain (coupled to the length of the gain medium and the pump power), and the gain depletion level (coupled to the number of round trips and to the seed energy). Therefore, varying these parameters allow to fine-adjust the spectral shaping effect and optimize the output pulses in terms of peak power and pulse quality.

We have chosen to analyze the effects of an intra-cavity etalon in a Ho:YLF regenerative amplifier to demonstrate the capability of our spectral simulation model. The underlying code, however, is not restricted to this particular system setup. Other types of spectral filters, either positioned intra-cavity or externally, can easily be integrated. Also the effect of different gain materials, with slightly miss-matched gain peaks, could be tackled. Finally, as our simulations compute consecutive pump and amplification cycles, a statistical analysis of the output pulses in terms of stability and bifurcation behavior is also in the scope of this simulation approach.

Appendix 1. Derivation of the inverted fraction updating equation

The following derivation bases on the monochromatic FN gain updating equation

$$g_i = g_{i-1} + \Delta g_i = g_{i-1} + \frac{\Delta J_{stor,i}}{J_{sat} l}, \quad (12)$$

which is, in the first step, reformulated to the monochromatic inverted fraction updating equation

$$\beta_i = \beta_{i-1} - \Delta \beta_i = \beta_{i-1} - \frac{\lambda \Delta J_i}{hc l N}. \quad (13)$$

The derived relationship between the change of inverted fraction $\Delta \beta_i$ and the change of fluence ΔJ_i allows us in the second step to generalize the monochromatic inverted fraction updating equation (Eq. 18) for the spectral regime (Eq. 20).

As the extracted and the stored fluence is related by

$$\Delta J_{stor} = J_{stor,i} - J_{stor,i-1} = -(J_i - J_{i-1}) = -\Delta J_i, \quad (14)$$

the gain updating Eq. (12) can be written as

$$g_i = g_{i-1} - \frac{\Delta J_i}{J_{sat} l}, \quad (15)$$

with the saturation fluence

$$J_{sat} = \frac{hc}{\lambda(\sigma_{em} + \sigma_{abs})}, \quad (16)$$

and the small signal gain g_x defined as a function of the inverted fraction β_x by

$$g_x = N(\beta_x(\sigma_{em} + \sigma_{abs}) - \sigma_{abs}), \quad (17)$$

the gain updating equation can be expressed as a function of β_i and β_{i-1} . Rearranging for β_i finally results in the inverted fraction updating equation

$$\beta_i = \beta_{i-1} - \frac{\lambda \Delta J_i}{hc l N} = \beta_{i-1} - \Delta \beta_i. \quad (18)$$

It can be seen, that the change of the inverted fraction $\Delta \beta_i$ is proportional to the expression $\lambda \Delta J_i$. Likewise interpreted for the chromatic case, the integration of the expression $\lambda \Delta J_i$ over the wavelength has to be proportional to the change of the inverted fraction

$$\Delta \beta_i \sim \int \lambda \Delta J_i(\lambda) d\lambda. \quad (19)$$

Finally, with $\Delta J_i(\lambda) = J_i(\lambda) - J_{i-1}(\lambda)$ and accounting for the single pass transmission $T(\lambda)$, the inverted fraction updating equation can be written as

$$\beta_i = \beta_{i-1} - \frac{\int \left[\lambda \left(\frac{J_i(\lambda)}{T(\lambda)} - J_{i-1}(\lambda) \right) \right] d\lambda}{hc l N}. \quad (20)$$

To further lay out the meaning of the previous expression we can use the change in the stored energy in the gain medium $\Delta E_i = \Delta J_i A$, with A as the laser beam area, and the energy of a single photon $E_{ph} = hc/\lambda$ to derive

$$\beta_i = \beta_{i-1} - \frac{\Delta E_i / E_{ph}}{N I A}. \quad (21)$$

The term $\Delta E/E_{ph}$ represents the change in the total number of photons ΔN_{ph} , and $N I A$ the total number of ions N_{total} in the considered gain volume. As the inverted fraction is defined as $\beta = n_e/N_{total}$ [11], with n_e representing the number of excited ions, we can write

$$\beta_i = \beta_{i-1} - \frac{\Delta N_{ph,i}}{N_{total}} = \beta_{i-1} + \frac{\Delta n_{e,i}}{N_{total}}. \quad (22)$$

This relation reveals that any decrease or increase of a propagating fluence by a certain number of photons inevitably leads to an increase or decrease of the same number of excited ions in the gain medium.

Appendix 2. Table of variables and constants

Table 1. Variables and Constants Used in This Paper

Symbol	Simulation parameter	Value used (if applicable)	Unit (if applicable)	Reference
Simulation code				
n_e	Number of excited ions			
N_{total}	Number of dopant ions in gain medium			
β	Inverted fraction			[11]
$G(\lambda)$	Spectral single pass gain			[15]
$g(\lambda)$	Spectral gain		m^{-1}	[15]
$\sigma_g(\lambda)$	Spectral gain cross section		m^2	[15]
$\sigma_{em}(\lambda)$	Spectral emission cross section		m^2	[12]
$\sigma_{abs}(\lambda)$	Spectral absorption cross section		m^2	[12]
τ_{gain}	Excited state life time	0.015	s	[12]
Δt	Time duration of fluence slice		s	
$J(\lambda)$	Spectral fluence		J/m^2	[15]
N	Dopant ion density in gain medium	$0.6 \cdot 10^{26}$ (0.5% doping)	m^{-3}	
l	Length of gain medium	0.04	m	
$T(\lambda)$	Single pass transmission	0.925		
h	Planck constant	$6.63 \cdot 10^{-34}$	J s	
c	Speed of light	$3 \cdot 10^8$	m/s	
Etalon parameters:				
R	Surface reflection			
L	Thickness		m	
Θ	Turning angle		degree	
n	Refractive index			
$T_{etalon}(\lambda)$	Spectral transmission of etalon			[18]
Pulse characterization:				
λ_{FWHM}	Spectral FWHM		m	
τ_{FWHM}	Temporal FWHM pulse duration		s	
τ_{rms}	Temporal rms pulse duration		s	[19]
NPC	Normalized pulse contrast			This paper
Appendix:				
J_{stor}	Stored fluence in gain medium		J/m^2	
E_{stor}	Stored energy in gain medium		J	
E_{ph}	Photon energy		J	
N_{ph}	Number of photons			

Acknowledgments

This work has been funded through the Max-Planck-Gesellschaft (Max-Planck Society). The authors thank Anne-Laure Calendron and Haider Zia for helpful discussions.